Ground-to-UAV, laser-based, multi-species emissions quantification at long standoff distances

Kevin C. Cossel[1*], Eleanor M. Waxman[1], Eli Hoenig[1], Daniel Hesselius[2], Christopher Chaote[2], Ian Coddington[1], Nathan R. Newbury[1]

5 [1]National Institute of Standards and Technology, Spectrum Technology and Research Division, Boulder, CO 80305, USA
[2]Integrated Remote and In-Situ Sensing (IRISS), University of Colorado, Boulder, CO 80305, USA

Correspondence to: Kevin C. Cossel (kevin.cossel@nist.gov)

Abstract. Determination of trace gas emissions from sources is critical for understanding and regulating air quality and climate change. Here, we demonstrate a method for rapid quantification of the emission rate of multiple gases from simple and complex

10 sources using a mass-balance approach with a spatially scannable open-path sensor – in this case, an open-path dual-comb spectrometer. The open-path spectrometer measures the total column density of gases between the spectrometer and a retroreflector mounted on an unmanned aerial vehicle (UAV). By measuring slant columns at multiple UAV altitudes downwind of a source (or sink), the total emission rate can be rapidly determined without the need for an atmospheric dispersion model. Here, we demonstrate this technique using controlled releases of CH_4 and C_2H_2. We show an emission rate

15 determination to within 50% of the known flux with a single 10-minute flight and within 10% of the known flux after 10 flights. Furthermore, we estimate a detection limit for CH_4 emissions to be 0.03 g CH_4/s. This detection limit is approximately the same as the emissions from 25 head of beef cattle and is less than the average emissions from a small oil field pneumatic controller. Other gases including CO_2, NH_3, HDO, ethane, formaldehyde (HCHO), CO, and N_2O can be measured by simply changing the dual-comb spectrometer.

20 ## 1 Introduction

Measurements of the emission rate of a gas or gases from point and area sources are important in a range of monitoring applications. Several examples include measurement of emissions of CH_4 and volatile organic compounds (VOCs) from oil and gas facilities (well pads, compressor stations, processing plants, etc.), from landfills and from composting facilities, CH_4 and N_2O (as well as VOCs) from waste-water treatment plants, CH_4, NH_3, and N_2O from agricultural sites, and VOCs from

25 industrial facilities. In all these examples, there are several important challenges for a measurement system. First, it is desirable to be able to measure emissions of multiple gases simultaneously. Second, the measurement system should be able to handle complex sources such as distributed sources or collocated sources. Finally, it is often desirable to be able to rapidly survey different sources to determine if emissions are present and then to quantify the emissions.

30 Because of the fundamental importance of emission rate measurements in monitoring and regulation, there are a wide range of different measurement methods that have been developed, all with distinct advantages and disadvantages. We cannot exhaustively review all the techniques here, but instead highlight a few general classes of techniques. First are the ground-based survey techniques with a point sensor (Vaughn et al., 2017; Zhang et al., 2019; Ravikumar et al., 2019; Riddick et al., 2022). One limitation of these techniques is that the vertical distribution of the gas is not measured, so assumptions need to be

35 made about the vertical and horizontal gas dispersion (using an atmospheric transport model). The transport assumptions can be removed by releasing a tracer gas co-located with the unknown emission source (Czepiel et al., 1996; Mønster et al., 2014; Roscioli et al., 2015); however, this requires access to and knowledge of the emission source. To circumvent these challenges, mass-balance approaches can be used by measuring in two dimensions which greatly relaxes the requirements on the transport model. Most frequently, mass-balance is performed using point sensors on aircraft (Alfieri et al., 2010; Conley et al., 2017;

40 Karion et al., 2013; White et al., 1976). While effective for large sources, challenges such as flight altitude restrictions, cost, and the requirement for fast sensors can limit applicability and repeat measurements. More recently, unmanned aerial vehicles (UAVs) have been used for small-scale mass balance (Gålfalk et al., 2021; Golston et al., 2018; Reuter et al., 2021; Zondlo, 2021), although not many sensors meet the precision as well as size, weight, and power requirements to deploy in this fashion. Long open-path measurements to a UAV were very recently used in conjunction with a Gaussian plume model to determine

45 an emission rate from a point source (Soskind et al., 2023). Finally, several mass-balance approaches have been demonstrated using column-integrated measurements including solar-occultation flux (which can only be used during daytime/sunny conditions) (Kille et al., 2017; Mellqvist et al., 2010) and airborne LiDAR (which has only been demonstrated for a few gases) (Ravikumar et al., 2019; Amediek et al., 2017; Bell et al., 2022; Kunkel et al., 2023).

50 Here, we demonstrate a new, mobile, micrometeorological mass-balance method using a line-integrated sensor (in this case, open-path dual-comb spectroscopy or DCS) in combination with an unmanned aerial vehicle. This is accomplished by measuring slant columns to a moving UAV that carries a small retroreflector downwind of an emission source as shown in Fig. 1. We test this technique using controlled releases of CH_4 and C_2H_2 from both a point source and a small area. A key strength of this technique – and other mass-balance techniques – is that it does not rely on a dispersion model. In principle this

55 approach is also compatible with any open-path laser measurement, such as tunable diode laser spectroscopy (Plant et al., 2015; Bailey et al., 2017; Dobler et al., 2017; Bai et al., 2022), but here we use a frequency comb to allow for simultaneous multispecies detection (Coddington et al., 2016; Cossel et al., 2021; Picqué and Hänsch, 2019). For example, while CH_4 and C_2H_2 measurements are demonstrated here, open-path dual-comb spectroscopy has been used to retrieve a host of interesting species including CO_2, NH_3, HDO, ethane, formaldehyde (HCHO), CO, and N_2O (Giorgetta et al., 2021; Herman et al., 2021;

60 Waxman et al., 2017; Ycas et al., 2019).

2 Experimental setup

This method builds on our previous demonstration of spatially-scanned DCS (Cossel et al., 2017), which is summarized in Figure 1(a). The primary components of the system (Figure 1b) are the dual frequency combs, a transmit/receive terminal that sends the light over a long open-air path, and a mobile reflector on a quadcopter.
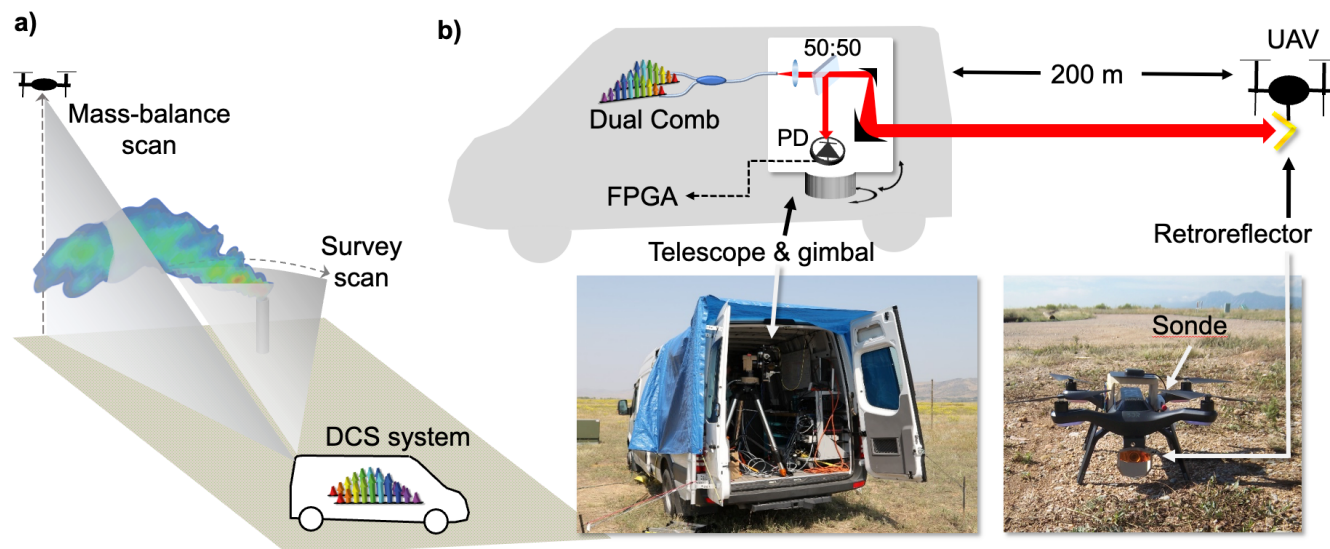
65

Figure 1. (a) Overview of experimental concept. The DCS system measures integrated slant columns to a moving UAV. By performing survey scans, the presence and angular position of an emissions source can be rapidly determined. Mass-balance scans downwind of the source then enable quantification of the emissions. (b) Details of experimental setup. The light from dual frequency combs is combined in fiber then launched out of a transmit/receive telescope system located on an azimuth/elevation gimbal to a
70 **retroreflector located on a UAV at a typical distance of 200 m. The return light from the retroreflector is separated with a 50:50 beamsplitter and measured on a photodetector (PD). This signal is digitized and averaged with a field-programmable gate array (FPGA)-based acquisition system. The lower part of (b) shows the van in the field as well as a photo of the UAV showing the retroreflector and sonde.**

75 Here, we use robust Er:fiber-based frequency combs operating in the near-infrared (Waxman et al., 2017). The design and operation of these combs has been described in detail previously (Truong et al., 2016). Briefly, the frequency combs have a nominal repetition rate of 200 MHz and a repetition rate difference of δf_{rep} = 625 Hz. The combs are both stabilized to a crystal oscillator and cw reference laser at 1560 nm to maintain mutual coherence between the combs. After amplification, spectral broadening, and spectral filtering to cover bands for C_2H_2 (1520 nm – 1540 nm) and CH_4 (1610 nm – 1670 nm), the light from
80 the two combs is combined in fiber and then is launched from a transmit/receive telescope (76.2-mm-diameter aperture) to a retroreflector (62.5-mm diameter) located on a UAV (here, a quadcopter). Return light from the retroreflector is collected with the same telescope and reflected off a 50:50 beamsplitter to a photodetector. Alignment to the retroreflector is maintained by an image-processing-based pointing servo using an 850-nm LED and Si CMOS camera co-aligned with the main telescope (Cossel et al., 2017). Figure 1(b) shows a more detailed view of the UAV. In addition to the retroreflector, the UAV also
85 carries several sondes to measure temperature, pressure, humidity, and GPS location, as well as real-time kinematic (RTK)

GPS for high-precision relative GPS location of the UAV. However, sufficient location precision was provided by the on-board GPS, so that is used for most of the data presented here. For field operations, the DCS system is housed in a van and connected via fiber to a telescope and fast azimuth-elevation gimbal located at the back of the van as pictured in Figure 1(b). Wind speed and direction were measured with a 3D sonic anemometer located away from the van at ~2 m above ground.

90 Additional meteorological parameters (temperature, pressure, independent wind speed and direction) were recorded by a weather station with a 2D sonic anemometer located above the van roof. This second wind measurement was used for redundancy and to verify the 3D sonic measurements. Finally, we measured CH_4 concentrations with a commercial cavity-ringdown spectrometer (CRDS) that sampled air from above the roof of the van. This spectrometer was calibrated at the NOAA Global Monitoring Laboratory to provide WMO-traceable CH_4 measurements, which we use to determine the background CH_4

95 concentration during flights.

The dual-comb signal on the receive photodetector is a time-domain interferogram (IGM) that repeats at a rate of δf_{rep}. We digitize this signal and co-add using a field-programmable gate array (FPGA). Sequential sets of 10,000 IGMs are coadded (with phase correction applied to each set of 100 sequential IGMs). In total this gives a 16s sampling period. In post processing,

100 each saved IGM was converted to a transmission spectrum (Figure 2(a)) via a Fourier transform and then fit with a spectral transmission model (calculated from HITRAN2008 (Rothman et al., 2009) using the measured temperatures and pressures) plus a piecewise polynomial baseline term to determine total column densities for three gases, CH_4, H_2O, and C_2H_2 along the laser path, $\bar{\rho}_g = \int_0^L \rho(x, y, z) dr$, where $\rho_g(x, y, z)$ is the spatially varying density of the gas and r is the position along the path (Waxman et al., 2017; Cossel et al., 2021). These total column densities are converted to path-averaged dry mixing ratios

105 for CH_4 and C_2H_2 reported in ppm (µmol/mol) or ppb (nmol/mol) using the temperature and pressure from the weather station, the temporally varying path length determined from the UAV GPS location, and the DCS-measured water vapor for the dry-air correction (Waxman et al., 2017). The measurement precision is characterized by the Allan-Werle deviation of the retrieved path-averaged concentration during one flight with no gas release (thus approximately uniform mixing ratios) as shown in Figure 2(b). For this flight, the number of co-added interferograms was reduced to 1000, resulting in measurements every 1.6

110 s. At the typical measurement time of 16 s, the CH_4 precision is around 10 ppm-m (25 ppb for a round-trip path length of 400 m). This performance is similar to that obtained from (Waxman et al., 2017) – 50 ppb extrapolated to the same measurement time and path length – indicating very little degradation due to motion of the UAV.
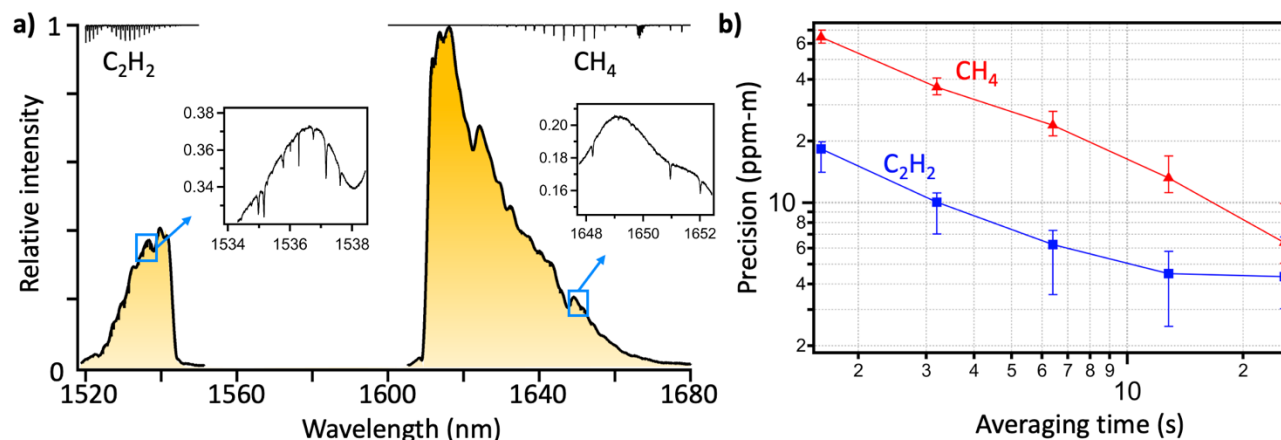
Figure 2. (a) Example normalized transmission spectrum (10-minute average). C$_2$H$_2$ is retrieved in the band around 1540 nm and CH$_4$ is retrieved in the band around 1640 nm. A simulated transmission spectrum for both gases is shown along the top to guide the eye. (b) Allan deviation of $\bar{\rho}_g$ for both CH$_4$ and C$_2$H$_2$ at ambient concentration from one flight. The round-trip path length was around 400 m.

Flights were performed across four different days. Each flight had a maximum duration of ~10 minutes. Several different flight patterns were used; here we focus on horizontal and vertical scans. The UAV was manually piloted for all the flights. Several different leak locations and arrangements were used in order to mimic emission sources that might be observed in the field. Controlled releases of CH$_4$ and C$_2$H$_2$ were located ~100 m from the van and were conducted using cylinders whose flow rate was either controlled with a mass flow controller or monitored with a flow meter. For CH$_4$, the flow rate was set around 0.22 g/s. For C$_2$H$_2$, the flow rate was set at around 0.18 g/s but was only used during a subset of releases. After the flow meter/controller, the gas was sent through a few-meter-long piece of PTFE tubing whose end was located between 0 m and ~5 m above ground level to simulate a point source emission. Small-area diffuse emissions were also simulated by puncturing the PTFE tubing every ~30 cm and placing the tubing on the ground across a ~2 m diameter area.

3 Results

3.1 Survey scan for emissions detection

We first demonstrate rapid detection of an emission source and later quantification of its emissions. For detection, the UAV is scanned horizontally at 200-m distance from the telescope – as illustrated by the dotted grey line in Fig. 1(a) – resulting in measurements across a series of near-horizontal slant paths. For this demonstration, the source emitted both CH$_4$ and C$_2$H$_2$ from a pole ~5 m above ground level (AGL) located ~100 m away from the launch/receive telescope.
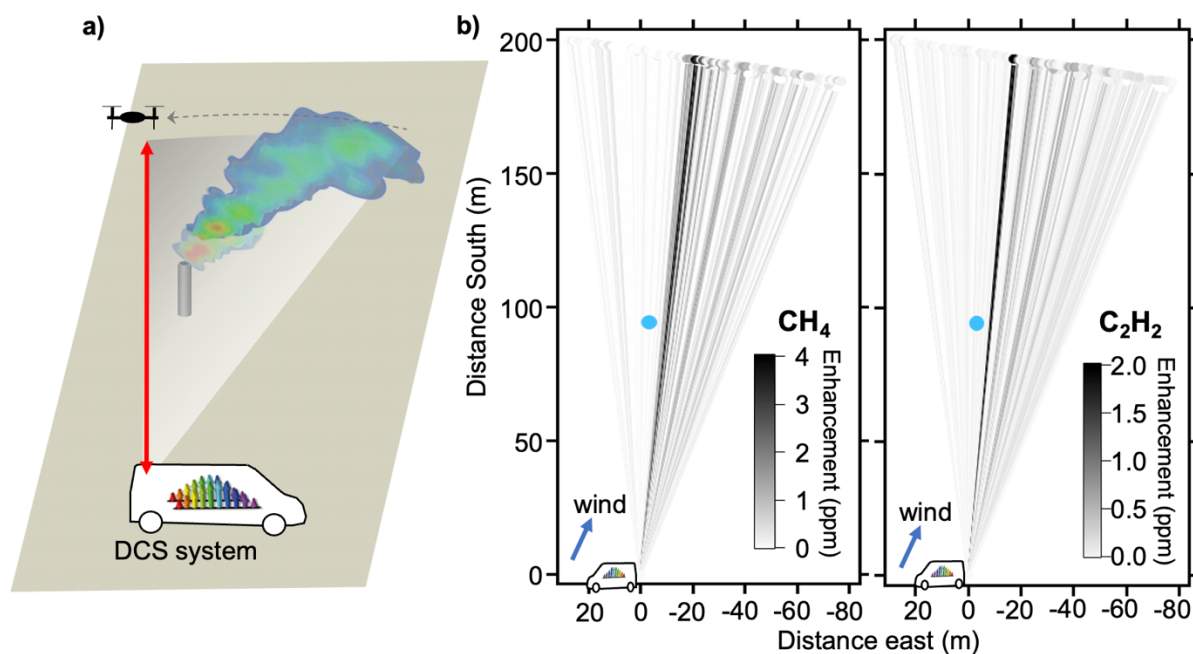
Figure 3. (a) Detection and location concept using a constant altitude horizontal scan. (b) Map of the results for CH$_4$ (left) and C$_2$H$_2$ (right) from a flight with both CH$_4$ and C$_2$H$_2$ releases. The van is located at (0,0) and the UAV relative position is shown by the dots. For this flight, two horizontal scans were completed at 5 m and 9 m AGL. The release location is shown by a blue dot, and the wind direction shown by a blue arrow. The release was at a height of ~2 m AGL, and the mean wind speed was 2 m/s. Each measurement path is shown by a solid line, shaded by the path-averaged CH$_4$ or C$_2$H$_2$ enhancement over background (see text for details). For both gases, a sudden increase in the enhancement is visible ~5 meters downwind of the leak source.

To analyze the results, we calculate the path-averaged enhanced column density ($\Delta\bar{\rho}_g$) for each gas g (CH$_4$ and C$_2$H$_2$), $\Delta\bar{\rho}_g = \bar{\rho}_g - L\langle\rho_g\rangle$, where $\bar{\rho}_g$ is the measured column density, L is the path length, and $\langle\rho_g\rangle$ is the mean background concentration. For CH$_4$, the background concentration is obtained from the dry mixing ratio from the CRDS using the known air temperature, pressure, and water vapor interpolated to the DCS data timestamp. For C$_2$H$_2$, the background concentration is set to the mean of the DCS measurements without any release. Figure 3(b) shows the CH$_4$ and C$_2$H$_2$ path-averaged concentration enhancement ($\Delta\bar{\rho}_g/L$) from a single flight consisting of two horizontal scans at different altitudes (scans at both altitudes are aggregated in one plot). As expected, we observe significant enhancements of CH$_4$ and C$_2$H$_2$ for slant paths when the UAV is immediately downwind of the emission location. The enhancements persist but decrease in amplitude as the paths move further downwind. Once the presence of an emissions source is detected with a horizontal scan, additional flights can be used for emissions quantification as discussed below. Further localization can be accomplished with more complex flight patterns (Soskind et al., 2023).

3.2 Mass-balance scan for emissions quantification

3.2.1 Methods

155   In order to perform emissions rate quantification, the UAV flew a vertical profile downwind of the emissions source as illustrated in in Figure 4(a). An example altitude profile recorded by the GPS on-board the UAV is shown as an inset. In this case, two vertical profiles between ~2 m and 30 m above ground level were performed during a single flight. Flights were also conducted with a single vertical scan during the flight. The flight patterns result in a series of measurements of the column density (or path-integrated concentration), $\bar{\rho}_g(z)$, for each gas species g and UAV height z with 16-s integration times.

160
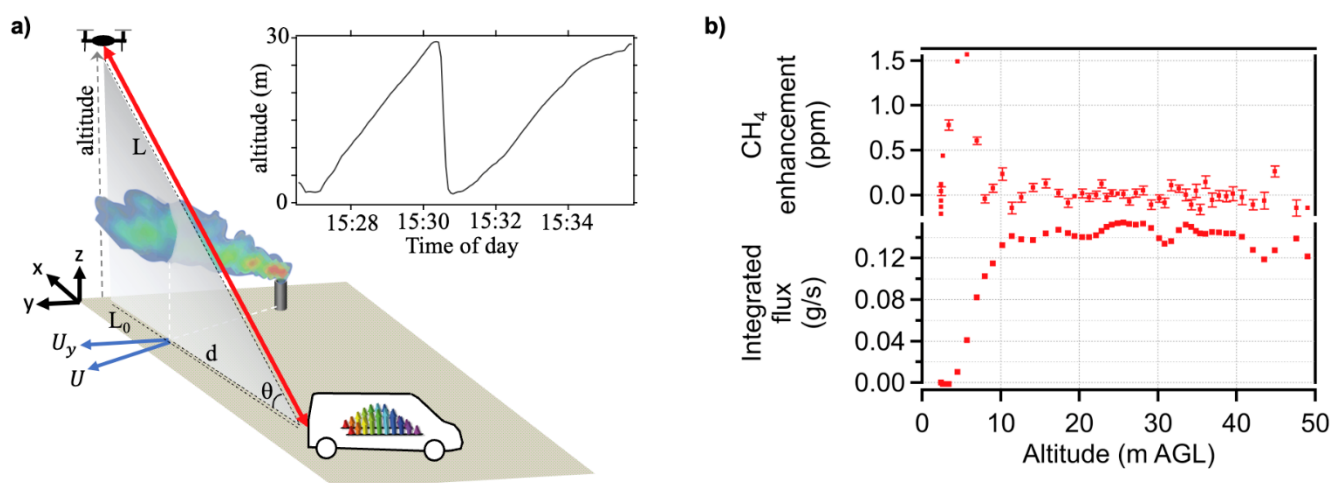
Figure 4. (a) Diagram of measurement configuration for flux determination from and emission source. The UAV is located a distance L **from the DCS system and is scanned vertically with altitude above ground level given by** z**. The DCS system measures a slant column from the comb system to the UAV and back, as the UAV slowly changes altitude. The plume is transported by the wind**
165 **vector denoted by** U **(with the component perpendicular to the measurement plane given by** U_y**) and intersects the measurement plane a distance** d **from the comb system. The inset shows an example UAV altitude profile (above ground level) for one flight. (b) Example data from one flight. (top panel) CH$_4$ enhancement above background versus UAV altitude. (bottom panel) Integrated flux versus altitude.**

170   To determine the flux, F, we start by following other mass-balance approaches (Alfieri et al., 2010; Karion et al., 2013; Mellqvist et al., 2010). With the geometry of Figure 4, we assume the x-axis is defined by the path from the telescope to the UAV position projected on the ground, and the z-axis is vertical. We can then write the flux through a closed surface S as

$$F = \oiint_S \Delta\rho(x, y, z)\boldsymbol{U} \cdot d\boldsymbol{A}, \tag{1}$$

where $\boldsymbol{U}$ is the wind velocity vector, with incremental area $d\boldsymbol{A}$ is the incremental area of the surface, and $\Delta\rho(x, y, z)$ is the gas
175 density above background. If we assume a significant y-component to the wind velocity vector, U_y, then the entire plume passes through the x-z plane. Thus, the total flux is found by integrating the enhanced concentration across the x-z plane or

$$F = \iint \Delta\rho(x,z)U_y \, dx \, dz \, . \tag{2}$$

However, because the DCS system is measuring a slant column between a fixed point and a moving point – $i.e.$, it measures $\Delta\bar{\rho}(r,\theta) = \int_0^L \Delta\rho(r,\theta) dr$ – we convert Equation (2) to polar coordinates and restrict the integrals to the plane shown in Figure 4(a) ($0 \leq \theta \leq \theta_{max}$), assuming that the end position of the UAV in both x and z coordinates lies beyond the plume. Then,

$$F = \int_0^{\theta_{max}} U_y \int_0^L \rho(r,\theta) r \, dr \, d\theta \tag{3}$$

Note the presence of the additional r term in the integral, which means that this integral is not directly what the DCS system measures. To evaluate this, we assume that $\rho(r,\theta) = \Delta\bar{\rho}(\theta)\delta(r - d/\cos\theta)$. That is, we assume the plume is localized to intersect the measurement plane at $x = d$. Then,

$$F = \int_0^{\theta_{max}} U_y \int_0^L \Delta\bar{\rho}(\theta)\delta\left(r - \frac{d}{\cos\theta}\right) r \, dr \, d\theta \, . \tag{4}$$

Evaluating the radial integral gives

$$F = \int_0^{\theta_{max}} U_y \Delta\bar{\rho}(\theta) \frac{d}{\cos\theta} \, d\theta \, . \tag{5}$$

Converting back to cartesian coordinates with $z = L_0 \tan\theta$ and assuming that $z \lesssim L/4$ gives finally

$$F \approx \frac{d}{L_0} \int_0^H U_y \Delta\bar{\rho}(z) dz \, , \tag{6}$$

where H is the maximum altitude. Equation (6) is derived for the delta-function plume but is valid for other plume shapes where d is defined using the mass-weighted mean. In addition, it assumes that d and L_0 are constant through one flight. We note the d/L_0 correction is unnecessary if both the launch and reflector could be moved together, in which case Equation (2) can be evaluated directly. We can intuitively understand the presence of the d/L_0 by looking again at a narrow plume intersecting the measurement plane at $x = d$. The effective altitude range at the plume is $\frac{d}{L_0}H$ instead of H, thus we need to do a change of variable to $z' = \frac{d}{L_0}z$ when doing the altitude integral.

To calculate the flux from a vertical scan, we first interpolate the auxiliary data (UAV location, wind speed and direction, CRDS CH_4) to the DCS data timestamp and filter the DCS data for low signal-to-noise ratio (for example, if the telescope tracking lost alignment briefly). Then, we determine $\Delta\bar{\rho}_g$ as in Section 3.1. Finally, Equation (6) is numerically integrated to obtain the total flux.

The result of the numerical integration of Equation (6) versus altitude is shown in the top panel of Fig. 4(b) for one flight. For this flight, the CH_4 enhancement profile shows a clear peak between 0 m and 10 m AGL, which corresponds to a rapid increase in the integrated flux. After 10 m AGL, the enhancement has dropped back to background levels and remains near background up to 50 m AGL. As expected from this enhancement profile, the integrated flux shows a steady increase from 0 m to 10 m AGL, after which it remains relatively constant up to 50 m. The variations between 10 m and 50 m are driven by

205 measurement noise and provide an estimate of the sensitivity of the flux determination. Note that any offset between the CRDS background and the DCS background would lead to a linear slope during this period from 10 m to 50 m, which is not observed in the measurements.

3.2.1 Results

210 Flights were performed across four different days. Approximately 20 vertical profile flights were conducted; however, on several flights, the wind direction was wrong or shifted early in the flight and caused the plume to miss the measurement path. We note that this information is known in the field from of the meteorological sensors, and the measurement can simply be repeated when the wind has stabilized. In addition, on one flight, the integrated flux was still increasing at the final altitude, indicating that slant path did not reach the top of the plume, so this flight was discarded from the analysis. In total, 14 flights

215 had sufficient data to determine a flux. Of these, four flights were performed with no release and were evaluated to determine "background" flux. Figure 5 shows a summary of the CH_4 flux determined for these flights.
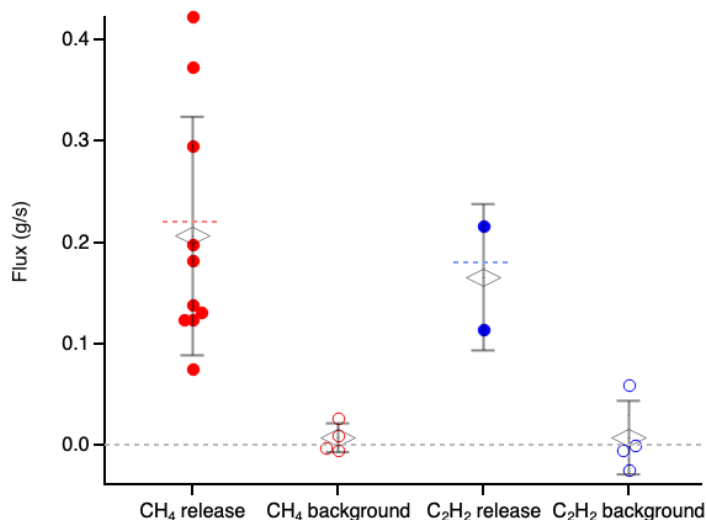
Figure 5. CH_4 and C_2H_2 flux determination for flights with a release and without a release ("background"). A single flight corresponds to a single point for CH_4 and for C_2H_2. For each set, the mean is shown by a diamond and the standard deviation
220 **indicated by the vertical lines. The CH_4 release rate was 0.22 g/s and the C_2H_2 rate was 0.18 g/s as indicated by the dashed horizontal lines.**

For the 10 flights with a CH_4 release, the mean flux determined was 0.21 ± 0.12 g/s to within one standard deviation. The mean agrees within 5% of the expected flux of 0.22 g/s, while the standard deviation indicates 50% uncertainty for a single flight. Of these 10 flights, four flights had a point release and six flights had a diffuse release, illustrating the capability to measure

225 both types of emissions. No obvious differences were observed for the two release types. For these flights, the distance of the measurement plane downwind from the source varied from ≈10 m to ≈60 m. The four background flights give a mean of

0.008±0.014 g/s. We estimate the detection limit for CH₄ fluxes as twice the deviation of these background flights, or about 0.03 g/s. For two flights, C₂H₂ was also released at 0.18 g/s with measured flux values of 0.14 g/s and 0.23 g/s, again in good agreement. The C₂H₂ background flights give a mean of 0.008±0.04 g/s.

230   3.2.2 Discussion

The uncertainty in the flux determination is a result of several contributions. First, we note the accuracy of the methane gas concentration measured by DCS is at the level of ~ 1% (Waxman et al., 2017) and is not a significant contribution. The uncertainty arises in the conversion of these measurements to a flux determination via Equation (6) due to several effects. First, incorrect measurement of the background gas concentrations (for example, due to biases between two CH₄ measurement systems) could lead to an error in $\Delta\bar{\rho}_g$ and a corresponding error in the flux. However, such a bias will result in a linear slope even without a gas flux. From the data in Figure 4(b) for altitudes >10 m, we see no evidence of a linear slope. This is also true in the background flights. Again, this is not surprising given the accuracy of both DCS and the cavity ringdown spectrometer used for the background gas measurements, and we conclude the evaluation of $\Delta\bar{\rho}_g$ is not a significant source of uncertainty.

240

Errors in U_y will lead to lead directly to errors in the determined flux. We estimate an upper limit on this error by comparing the two different wind sensors. Their values of U_y averaged over a 10-minute flight agree to within ±20% and typically better. The difference is dominated by uncertainty in the wind speed, rather than the wind direction, given the geometry chosen here where the plume is approximately normal to the measurement plane. (The uncertainty in the wind direction is however important below in the determination of d.) The difference in U_y between the anemometers is likely due to true wind differences at the location of the wind sensors. It is possible that a UAV-based wind measurement could reduce this error and improve the flux determination.

Finally, there are three sources of uncertainty associated with the value of d in Eq (1). First, errors in the source location will cause errors in the determination of d. Assuming a random source location uncertainty of Δx, the corresponding uncertainty in d will also be Δx. For the measurements here, the source location was known to better than 1 m, so this uncertainty is negligible. In the case of an initially unknown source location, the approximate location will need to be determined well enough to meet the target accuracy goals based on the measurement configuration. For example, to keep this uncertainty below ±20%, the source location needs to be known to within ±0.2d. For the flights here with $d \approx 100$ m, the location would need to be known within ±20 m. In the case of a uniform diffuse source, the effective weighted center of the source needs to be known to this level. Second, even with a known source location, uncertainty in the wind direction $\Delta\phi$ will also lead to an uncertainty in d. There are two potential sources of wind direction errors: a static bias during one measurement between the measured wind direction at the sensor and the actual wind direction along the plume trajectory, and a temporally varying difference between

260 them. A static bias over one flight will lead to an error given by $\Delta\phi \times d_{dw}$, where d_{dw} is the downwind distance between the source and the measurement plane. Following the geometry here, the downwind distances are <50 m, so that a ±30˚ wind direction error (estimated from the mean difference between the two anemometers during different flights) corresponds to ±25 m error in d or ±25% error in the flux for $d = 100$ m. To investigate the impact of the within-flight variability, we recalculated the flux using a time-varying value of d (i.e. mapping d to a slowly varying function $d(z)$ within Eq. (6) using the known values of UAV altitude z as a function of time). For the 10 CH$_4$ release flights, the change in flux was in all cases <13%, with

265 a change in the mean value of 1.4%, indicating that the impact of temporally varying wind direction differences is minimal. As mentioned above, the static bias could be reduced by measuring the wind direction at the UAV itself. Furthermore, these wind direction related errors are minimized with longer measurement paths, which also help to reduce the impact of source location uncertainties. Third and finally, the use of d in Eq (1) relied on the assumption the weighted centroid of the plume followed the wind direction from the source to the measurement plane. Plume dynamics are complex and there is some

270 inherent uncertainty in the plume evolution over time. As an estimate of this effect, we assume that the plume centroid is offset on average by at most σ_y from the expected location based on the mean wind direction. The value of σ_y can be taken as the average beam spread in a Gaussian plume model (Seinfeld and Pandis, 2006). For typical daytime conditions with high solar insolation and ~2 m/s wind speeds (stability class 'A'), $\sigma_y \approx 15$ m, which corresponds to a ±15% error for $d = 100$ m. The combination of the assumed 20% uncertainty from the source location, 25% uncertainty from the wind direction, and 15%

275 uncertainty from the plume location yields a total ~35% uncertainty related to d.

As shown by the background flights, the uncertainty due to DCS measurement noise is expected to contribute ±6% for a flux of 0.22 g/s. So, when combined, the ±20% uncertainties associated with the values of U_y and ±35% uncertainty in d, we estimate a total estimated uncertainty of ~±41% in the measured flux values for a single flight. This estimated uncertainty is

280 reasonably close to the observed ±50%: differences between the two could be attributed to either poor determination of the observed variability due to small sample sizes or additional plume variability that was not accounted for in the estimates. Finally, we note that the uncertainties in U_y and d described above are statistical (driven by atmospheric variability and plume dynamics), thus are expected to average down with multiple measurements, as observed here with the low mean bias in the flux determination.

285 **4 Conclusions**

We have demonstrated a rapid mass-balance method for flux determination using path-integrated slant column measurements between a ground-based measurement system and a UAV located at varying heights above ground. A key advantage of this methodology is that no atmospheric dispersion model is needed. Using a near-infrared dual-comb spectroscopy system, we show flux quantification of CH$_4$ to within 50% with a single <10 min flight and an estimated detection limit of 0.03 g/s (2

290 sigma), which would enable detection of emissions from 25 head of cattle or from a single pneumatic controller. It is estimated

that 90% of all oil field emissions come from sources that are ten times larger than this limit (Brandt et al., 2016). We can also simultaneously determine C_2H_2 fluxes with similar performance. The methodology is flexible, so can be used to determine fluxes for any gas that can be measured with an open-path dual-comb spectroscopy or other open-path spectroscopy such as active differential optical absorption spectroscopy (Stutz et al., 2016). For example, CO_2, NH_3, HDO, ethane, formaldehyde

295 (HCHO), CO, and N_2O have all been measured with DCS (Giorgetta et al., 2021; Herman et al., 2021; Waxman et al., 2017; Ycas et al., 2019). In addition, with further engineering of mobile DCS, measurements could be conducted from a moving van, allowing for flexible and rapid coverage of a wide area.

Data Availability.

Data available from the authors on request.

300 *Author Contributions.*

K.C. and E.M. collected and analyzed the data. E.H. assisted with the field measurements and data collection from the UAV. D.H. and C.C. piloted the UAV. K.C., E.M., I.C., and N.N. wrote and edited the manuscript.

Competing Interests.

The contact author has declared that none of the authors has any competing interests.

305 *Acknowledgements.*

We thank Michael Cermak for technical assistance, Tim Newberger and Kathryn McCain from NOAA for assistance with the point sensor calibration, and Nathan Malarich, Ryan Cole, and Jerome Genest for helpful discussions on the manuscript.

Financial Support.

National Institute of Standards and Technology (NIST); DARPA Defence Sciences Office.

310

References

Alfieri, S., Amato, U., Carfora, M. F., Esposito, M. and Magliulo, V.: Quantifying trace gas emissions from composite landscapes: A mass-budget approach with aircraft measurements, Atmospheric Environment, 44(15), 1866–1876, doi:10.1016/j.atmosenv.2010.02.026, 2010.

315 Amediek, A., Ehret, G., Fix, A., Wirth, M., Büdenbender, C., Quatrevalet, M., Kiemle, C. and Gerbig, C.: CHARM-F—a new airborne integrated-path differential-absorption lidar for carbon dioxide and methane observations: measurement performance and quantification of strong point source emissions, Applied Optics, 56(18), 5182, doi:10.1364/AO.56.005182, 2017.

Bai, M., Loh, Z., Griffith, D. W. T., Turner, D., Eckard, R., Edis, R., Denmead, O. T., Bryant, G. W., Paton-Walsh, C., Tonini, M., McGinn, S. M. and Chen, D.: Performance of open-path lasers and Fourier transform infrared spectroscopic systems in agriculture emissions research, Atmospheric Measurement Techniques, 15(11), 3593–3610, doi:10.5194/amt-15-3593-2022, 2022.

Bailey, D. M., Adkins, E. M. and Miller, J. H.: An open-path tunable diode laser absorption spectrometer for detection of carbon dioxide at the Bonanza Creek Long-Term Ecological Research Site near Fairbanks, Alaska, Appl. Phys. B, 123(9), 245, doi:10.1007/s00340-017-6814-8, 2017.

Bell, C., Rutherford, J., Brandt, A., Sherwin, E., Vaughn, T. and Zimmerle, D.: Single-blind determination of methane detection limits and quantification accuracy using aircraft-based LiDAR, Elementa: Science of the Anthropocene, 10(1), 00080, doi:10.1525/elementa.2022.00080, 2022.

Brandt, A. R., Heath, G. A. and Cooley, D.: Methane Leaks from Natural Gas Systems Follow Extreme Distributions, Environ. Sci. Technol., 50(22), 12512–12520, doi:10.1021/acs.est.6b04303, 2016.

Coddington, I., Newbury, N. and Swann, W.: Dual-comb spectroscopy, Optica, 3(4), 414–426, doi:10.1364/OPTICA.3.000414, 2016.

Conley, S., Faloona, I., Mehrotra, S., Suard, M., Lenschow, D. H., Sweeney, C., Herndon, S., Schwietzke, S., Pétron, G., Pifer, J., Kort, E. A. and Schnell, R.: Application of Gauss's theorem to quantify localized surface emissions from airborne measurements of wind and trace gases, Atmos. Meas. Tech., 10(9), 3345–3358, doi:10.5194/amt-10-3345-2017, 2017.

Cossel, K. C., Waxman, E. M., Giorgetta, F. R., Cermak, M., Coddington, I. R., Hesselius, D., Ruben, S., Swann, W. C., Truong, G.-W., Rieker, G. B. and Newbury, N. R.: Open-path dual-comb spectroscopy to an airborne retroreflector, Optica, 4(7), 724–728, doi:10.1364/OPTICA.4.000724, 2017.

Cossel, K. C., Waxman, E. M., Baumann, E., Giorgetta, F. R., Coburn, S. C., Alden, C. B. and Washburn, B. R.: 2 - Remote sensing using open-path dual-comb spectroscopy, in Advances in Spectroscopic Monitoring of the Atmosphere, edited by W. Chen, D. S. Venables, and M. W. Sigrist, pp. 27–93, Elsevier., 2021.

Czepiel, P. M., Mosher, B., Harriss, R. C., Shorter, J. H., McManus, J. B., Kolb, C. E., Allwine, E. and Lamb, B. K.: Landfill methane emissions measured by enclosure and atmospheric tracer methods, Journal of Geophysical Research: Atmospheres, 101(D11), 16711–16719, doi:10.1029/96JD00864, 1996.

Dobler, J. T., Zaccheo, T. S., Pernini, T. G., Blume, N., Broquet, G., Vogel, F., Ramonet, M., Braun, M., Staufer, J., Ciais, P. and Botos, C.: Demonstration of spatial greenhouse gas mapping using laser absorption spectrometers on local scales, JARS, JARSC4, 11(1), 014002, doi:10.1117/1.JRS.11.014002, 2017.

Gålfalk, M., Nilsson Påledal, S. and Bastviken, D.: Sensitive Drone Mapping of Methane Emissions without the Need for Supplementary Ground-Based Measurements, ACS Earth Space Chem., 5(10), 2668–2676, doi:10.1021/acsearthspacechem.1c00106, 2021.

Giorgetta, F. R., Peischl, J., Herman, D. I., Ycas, G., Coddington, I., Newbury, N. R. and Cossel, K. C.: Open-Path Dual-Comb Spectroscopy for Multispecies Trace Gas Detection in the 4.5–5 μm Spectral Region, Laser & Photonics Reviews, 15(9), 2000583, doi:10.1002/lpor.202000583, 2021.

Golston, L. M., Aubut, N. F., Frish, M. B., Yang, S., Talbot, R. W., Gretencord, C., McSpiritt, J. and Zondlo, M. A.: Natural Gas Fugitive Leak Detection Using an Unmanned Aerial Vehicle: Localization and Quantification of Emission Rate, Atmosphere, 9(9), 333, doi:10.3390/atmos9090333, 2018.

Herman, D. I., Weerasekara, C., Hutcherson, L. C., Giorgetta, F. R., Cossel, K. C., Waxman, E. M., Colacion, G. M., Newbury, N. R., Welch, S. M., DePaola, B. D., Coddington, I., Santos, E. A. and Washburn, B. R.: Precise multispecies agricultural gas flux determined using broadband open-path dual-comb spectroscopy, Sci Adv, 7(14), eabe9765, doi:10.1126/sciadv.abe9765, 2021.

360   Karion, A., Sweeney, C., Pétron, G., Frost, G., Michael Hardesty, R., Kofler, J., Miller, B. R., Newberger, T., Wolter, S., Banta, R., Brewer, A., Dlugokencky, E., Lang, P., Montzka, S. A., Schnell, R., Tans, P., Trainer, M., Zamora, R. and Conley, S.: Methane emissions estimate from airborne measurements over a western United States natural gas field, Geophys. Res. Lett., 40(16), 4393–4397, doi:10.1002/grl.50811, 2013.

Kille, N., Baidar, S., Handley, P., Ortega, I., Sinreich, R., Cooper, O. R., Hase, F., Hannigan, J. W., Pfister, G. and Volkamer, 365   R.: The CU mobile Solar Occultation Flux instrument: structure functions and emission rates of NH_3, NO_2 and C_2H_6, Atmos. Meas. Tech., 10(1), 373–392, doi:10.5194/amt-10-373-2017, 2017.

Kunkel, W., Thorpe, M., Carre-Burritt, A., Aivazian, G., Snow, N., Harris, J., Mueller, T. and Roos, P.: Extension of Methane Emission Rate Distribution for Permian Basin Oil and Gas Production Infrastructure by Aerial LiDAR, [online] Available from: https://eartharxiv.org/repository/view/4895/ (Accessed 17 February 2023), 2023.

370   Mellqvist, J., Samuelsson, J., Johansson, J., Rivera, C., Lefer, B., Alvarez, S. and Jolly, J.: Measurements of industrial emissions of alkenes in Texas using the solar occultation flux method, J. Geophys. Res., 115(D7), D00F17, doi:10.1029/2008JD011682, 2010.

Mønster, J. G., Samuelsson, J., Kjeldsen, P., Rella, C. W. and Scheutz, C.: Quantifying methane emission from fugitive sources by combining tracer release and downwind measurements – A sensitivity analysis based on multiple field surveys, Waste 375   Management, 34(8), 1416–1428, doi:10.1016/j.wasman.2014.03.025, 2014.

Picqué, N. and Hänsch, T. W.: Frequency comb spectroscopy, Nature Photon, 13(3), 146–157, doi:10.1038/s41566-018-0347-5, 2019.

Plant, G., Nikodem, M., Mulhall, P., Varner, R. K., Sonnenfroh, D. and Wysocki, G.: Field Test of a Remote Multi-Path CLaDS Methane Sensor, Sensors, 15(9), 21315–21326, doi:10.3390/s150921315, 2015.

380   Ravikumar, A. P., Sreedhara, S., Wang, J., Englander, J., Roda-Stuart, D., Bell, C., Zimmerle, D., Lyon, D., Mogstad, I., Ratner, B. and Brandt, A. R.: Single-blind inter-comparison of methane detection technologies – results from the Stanford/EDF Mobile Monitoring Challenge, Elem Sci Anth, 7(1), 37, doi:10.1525/elementa.373, 2019.

Reuter, M., Bovensmann, H., Buchwitz, M., Borchardt, J., Krautwurst, S., Gerilowski, K., Lindauer, M., Kubistin, D. and Burrows, J. P.: Development of a small unmanned aircraft system to derive CO_2 emissions of anthropogenic point sources, 385   Atmospheric Measurement Techniques, 14(1), 153–172, doi:10.5194/amt-14-153-2021, 2021.

Riddick, S. N., Ancona, R., Mbua, M., Bell, C. S., Duggan, A., Vaughn, T. L., Bennett, K. and Zimmerle, D. J.: A quantitative comparison of methods used to measure smaller methane emissions typically observed from superannuated oil and gas infrastructure, Atmospheric Measurement Techniques, 15(21), 6285–6296, doi:10.5194/amt-15-6285-2022, 2022.

Roscioli, J. R., Yacovitch, T. I., Floerchinger, C., Mitchell, A. L., Tkacik, D. S., Subramanian, R., Martinez, D. M., Vaughn, 390   T. L., Williams, L., Zimmerle, D., Robinson, A. L., Herndon, S. C. and Marchese, A. J.: Measurements of methane emissions from natural gas gathering facilities and processing plants: measurement methods, Atmos. Meas. Tech., 8(5), 2017–2035, doi:10.5194/amt-8-2017-2015, 2015.

Rothman, L. S., Gordon, I. E., Barbe, A., Benner, D. C., Bernath, P. E., Birk, M., Boudon, V., Brown, L. R., Campargue, A., Champion, J. P., Chance, K., Coudert, L. H., Dana, V., Devi, V. M., Fally, S., Flaud, J. M., Gamache, R. R., Goldman, A.,
395 Jacquemart, D., Kleiner, I., Lacome, N., Lafferty, W. J., Mandin, J. Y., Massie, S. T., Mikhailenko, S. N., Miller, C. E., Moazzen-Ahmadi, N., Naumenko, O. V., Nikitin, A. V., Orphal, J., Perevalov, V. I., Perrin, A., Predoi-Cross, A., Rinsland, C. P., Rotger, M., Simeckova, M., Smith, M. A. H., Sung, K., Tashkun, S. A., Tennyson, J., Toth, R. A., Vandaele, A. C. and Vander Auwera, J.: The HITRAN 2008 molecular spectroscopic database, J. Quant. Spectrosc.Radiat. Transfer, 110(9–10), 533–572, doi:10.1016/j.jqsrt.2009.02.013, 2009.

400 Seinfeld, J. H. and Pandis, S. N.: Atmospheric Chemistry and Physics: From Air Pollution to Climate Change, Wiley., 2006.

Soskind, M. G., Li, N. P., Moore, D. P., Chen, Y., Wendt, L. P., McSpiritt, J., Zondlo, M. A. and Wysocki, G.: Stationary and drone-assisted methane plume localization with dispersion spectroscopy, Remote Sensing of Environment, 289, 113513, doi:10.1016/j.rse.2023.113513, 2023.

Stutz, J., Hurlock, S. C., Colosimo, S. F., Tsai, C., Cheung, R., Festa, J., Pikelnaya, O., Alvarez, S., Flynn, J. H., Erickson, M.
405 H. and Olaguer, E. P.: A novel dual-LED based long-path DOAS instrument for the measurement of aromatic hydrocarbons, Atmospheric Environment, 147(Supplement C), 121–132, doi:10.1016/j.atmosenv.2016.09.054, 2016.

Truong, G.-W., Waxman, E. M., Cossel, K. C., Baumann, E., Klose, A., Giorgetta, F. R., Swann, W. C., Newbury, N. R. and Coddington, I.: Accurate frequency referencing for fieldable dual-comb spectroscopy, Opt. Express, OE, 24(26), 30495–30504, doi:10.1364/OE.24.030495, 2016.

410 Vaughn, T. L., Bell, C. S., Yacovitch, T. I., Roscioli, J. R., Herndon, S. C., Conley, S., Schwietzke, S., Heath, G. A., Pétron, G. and Zimmerle, D.: Comparing facility-level methane emission rate estimates at natural gas gathering and boosting stations, Elem Sci Anth, 5(0), 71, doi:10.1525/elementa.257, 2017.

Waxman, E. M., Cossel, K. C., Truong, G.-W., Giorgetta, F. R., Swann, W. C., Coburn, S., Wright, R. J., Rieker, G. B., Coddington, I. and Newbury, N. R.: Intercomparison of open-path trace gas measurements with two dual-frequency-comb
415 spectrometers, Atmos. Meas. Tech., 10(9), 3295–3311, doi:10.5194/amt-10-3295-2017, 2017.

White, W. H., Anderson, J. A., Blumenthal, D. L., Husar, R. B., Gillani, N. V., Husar, J. D. and Wilson, W. E.: Formation and transport of secondary air pollutants: ozone and aerosols in the St. Louis urban plume, Science, 194(4261), 187–189, doi:10.1126/science.959846, 1976.

Ycas, G., Giorgetta, F. R., Cossel, K. C., Waxman, E. M., Baumann, E., Newbury, N. R. and Coddington, I.: Mid-infrared
420 dual-comb spectroscopy of volatile organic compounds across long open-air paths, Optica, 6(2), 165–168, doi:10.1364/OPTICA.6.000165, 2019.

Zhang, E. J., Teng, C. C., van Kessel, T. G., Klein, L., Muralidhar, R., Wysocki, G. and Green, W. M. J.: Field Deployment of a Portable Optical Spectrometer for Methane Fugitive Emissions Monitoring on Oil and Gas Well Pads, Sensors, 19(12), 2707, doi:10.3390/s19122707, 2019.

425 Zondlo, M. A.: 6 - Unmanned aerial systems for trace gases, in Advances in Spectroscopic Monitoring of the Atmosphere, edited by W. Chen, D. S. Venables, and M. W. Sigrist, pp. 321–343, Elsevier., 2021.